



Synthesis of high-efficiency phosphatized catalysts by using organophosphorus and biomass for photocatalytic hydrogen peroxide production via oxygen reduction

Yinglong Lu^{a,1}, Xin Yue^{b,c,1}, JunJie Cai^{c,1}, Xi He^a, Lejing Li^e, Quan Zhou^a, Chengyu Duan^a, Ruilin Wang^a, Mengdi Sun^a, Zheshun Ou^a, Huimin Liu^a, Guanghui Luo^a, Xiaoli Wang^a, Jimmy C. Yu^d, Zhuofeng Hu^{a,*}

^a School of Environmental Science and Engineering, Guangdong Provincial Key Laboratory of Environmental Pollution Control and Remediation Technology, Sun Yat-sen University, Guangzhou 510006, China

^b Guangzhou Key Laboratory of Low-Dimensional Materials and Energy Storage Devices, Collaborative Innovation Center of Advanced Energy Materials, Guangdong University of Technology, Guangzhou 510006, China

^c School of Materials and Energy, Guangdong University of Technology, Guangzhou 510006, China

^d Department of Chemistry, The Chinese University of Hong Kong, Shatin, New Territories, Hong Kong Special Administrative Region

^e Analytical Chemistry - Center for Electrochemical Sciences (CES), Faculty of Chemistry and Biochemistry, Ruhr University Bochum, Universitätsstr. 150, D-44780 Bochum, Germany

ARTICLE INFO

Keywords:

H₂O₂
Organophosphorus
Oxygen activation
P-HTCC
Photocatalyst

ABSTRACT

Transferring biomass waste into valuable catalysts has attracted extensive attention. Currently, biomasses are often contaminated via organophosphorus (OP) pesticides. Simultaneous conversion of agriculture waste and OPs into value products is a promising method. Herein, we propose a new strategy to transfer OPs-contaminated biomass into phosphorus-containing carbonaceous hydrothermal carbon (P-HTCC) catalysts. The hazardous organophosphorus will be transferred to phosphate and incorporated into the structure of HTCC. By using solar energy, this P-HTCC can reduce O₂ to form H₂O₂. The phosphorus element raises the conduction band, twists the polychains, and lowers the electron transfer resistance of the catalysts. Also, DFT calculation indicates that the phosphorus element will optimize the structure of HTCC and make the reaction more thermodynamically favorable. Finally, the P-HTCC can generate H₂O₂ to degrade organic pollutants like Ibuprofen. This work provides a new method for simultaneous treatment of organophosphorus and biomasses, and provides a new method for H₂O₂ generation.

1. Introduction

Organophosphorus (OP) has been widely used in pesticides [1], herbicides [2], plasticizers [3], flame retardants [4], etc., bringing huge economic benefits to human beings. However, they are easily released into the environment during production and/or through leaching, attrition, use, disposal, and recycling processes from the products, causing serious pollution to the environment, which poses a huge threat to human health [5]. European Union listed three new emerging pollutants, tris (2-chloroethyl) phosphate, tris (2-chloroisopropyl) phosphate, and tris (1,3-dichloroisopropyl) phosphate, as the fourth batch of

high-concern substances [6]. The Guangdong-Hong Kong-Macao Greater Bay Area in China is also seriously polluted by OP flame retardants, with the highest total concentration reaching 1032.7 ng·L⁻¹ [7].

OPs would migrate in different environmental media and have been detected in various environmental compartments [8]. They are insufficiently degraded in sewage treatment plants and enter the aquatic environment. Using it as a pesticide, it is found that many plants contain OPs. Currently, agriculture waste such as straw is often contaminated by OPs and this renders their treatment complicated. The extensive use of OP pesticides has resulted in residues found in most crops, which

* Corresponding author.

E-mail address: huzhf8@mail.sysu.edu.cn (Z. Hu).

¹ Yinglong Lu, Xin Yue and JunJie Cai contributes equally to this work.

<https://doi.org/10.1016/j.apcatb.2024.123771>

Received 7 October 2023; Received in revised form 9 January 2024; Accepted 21 January 2024

Available online 23 January 2024

0926-3373/© 2024 Elsevier B.V. All rights reserved.

accumulate through the precipitation of humus, phytoplankton and bacteria to form biogenic phosphorus [9]. In the countryside, if the OPs-containing agriculture is burned, they will produce plenty of harmful substrates like small particles and greenhouse gas, which will carry the OPs to spread to other places. Also, raining will also cause the OPs to migrate from the agricultural waste to other places and cause more pollutants. Therefore, how to treat the OPs-contaminated agriculture waste is of significance.

Currently, transferring agriculture into other valuable products is an important strategy for their treatment. In our opinion, the simultaneous conversion of agriculture waste and OPs into value products should be a promising method for the treatment of OPs-contaminated agriculture waste. Actually, agriculture waste usually contains cellulose, lignin and carbohydrate. Recently, it is discovered that those materials are able to be converted to hydrothermal carbonaceous carbon (HTCC) [10–13]. Cellulose and carbohydrate will undergo a dehydration and polymerization process and finally form a sp^2 -conjugated hybrid structure. Interestingly, the HTCC exhibits a semiconductor property. Under solar illumination, it is also able to produce photoexcited electrons, which can reduce oxygen into hydrogen peroxide (H_2O_2) [14] in pure water without adding any sacrificial agent [15].

It is well known that H_2O_2 is considered to be the greenest and the most environmentally friendly oxidant because its by-products are only water and oxygen [16,17]. It is widely used in disinfection, chemical synthesis, environmental remediation, papermaking, and fuel cells [18,19,20]. Currently, more than 95% of global H_2O_2 production is based on the anthraquinone process first developed in the 1940s. Although the produced H_2O_2 is concentrated up to 70 wt%, the process requires complex large-scale infrastructure and expensive palladium-based hydrogenation catalysts and involves a series of tedious steps (e.g., hydrogenation, oxidation, extraction, purification, and transportation). A large amount of toxic organic by-products are produced in the process, and the H_2O_2 produced must be transported over long distances and stored for a long time, which is very time-consuming and energy-intensive [21,22]. Other H_2O_2 production methods, such as one-step synthesis of H_2O_2 from H_2 and O_2 via noble metal catalysts, have low catalytic efficiency and potential explosion risks, while electrochemically synthesized H_2O_2 is also limited by its high energy consumption [23]. Therefore, the production of H_2O_2 via using HTCC transferred from agricultural waste is a very interesting topic because it is a green, energy-saving and sustainable technology that utilizes solar energy, oxygen and water for in-situ generation of H_2O_2 .

In our opinion, transferring agricultural waste is more complicated than pure cellulose and carbohydrate. In the case of OPs-containing agriculture waste, we propose that the key element of OPs is phosphorus and this will greatly influence the structure and activity of photocatalysts. For example, previous studies on P-doped $g-C_3N_4$ photocatalysts pointed out that the P element can adjust the energy band structure and expand the absorption range of visible light, thereby promoting the separation of photogenerated charges and improving the photocatalytic performance. This is because the lone pair of electrons of P can be delocalized from the P atom to the p-conjugated triazine ring to form an electron-rich state, and its empty 3d orbital shell can induce a large difference in charge density in the carbon matrix and can accommodate O_2 lone for electrons [24,25]. Yang et al. [26] synthesized P-doped mesoporous carbon (P-pOMC) as a metal-free catalyst for electrocatalytic oxygen reduction. The results of XPS analysis indicated that P-C bonds and P-O bonds covalently bound to the carbon skeleton were successfully formed. P-pOMC also exhibited excellent oxygen reduction activity, very close to the Pt/C catalyst, with 3.8 electrons transferred per O molecule. In addition, phosphorus can also be used as an oxophilic element to be doped with materials, thereby promoting the oxygen reduction ability in the air and improving the photocatalytic H_2O_2 production performance [27]. Zhang et al. [28] found that the addition of phosphorus increased the yield of H_2O_2 by a factor of 3.2 compared to pure bulk $g-C_3N_4$. However, there are no relevant studies

on the effect of P on H_2O_2 production from HTCC photocatalysts.

In this work, we first attempt to simultaneously convert organic phosphorus and biomass of cellulose to form phosphorus-containing HTCC through a simple hydrothermal method, and apply them to produce H_2O_2 in pure water by using solar energy. We study its photocatalytic oxygen reduction and H_2O_2 production performance. The effects of P on the electronic structure, energy band, carrier density, photogenerated charge transfer, photocatalytic performance, adsorption and activation of oxygen molecules, and hydrogen peroxide yield of HTCC will be systematically analyzed. It is found that OPs can introduce phosphorus element into the HTCC and remarkably enhance its activity. DFT calculation indicates that the phosphorus element will optimize the structure of HTCC and render the generation of H_2O_2 more thermodynamically favorable. This study points out a new strategy for the simultaneous treatment of OPs and agriculture and also provides a high-efficient material for H_2O_2 production.

2. Experimental section

2.1. Reagents

All solutions were prepared using deionized water and reagent-grade chemicals. IBU (purity > 98%), cellulose (particle size = 25 μm), p-benzoquinone (p-BQ, purity \geq 97%), tert-butanol (TBA, purity \geq 99.5%). N, N'-diethyl-p-phenylenediamine (DPD, purity \geq 98%), horseradish peroxidase (POD, specific activity of 100 units mg^{-1}). 5, 5-dimethyl-1-pyrroline-N-oxide (DMPO, purity \geq 98%) was purchased from Sigma-Aldrich.

2.2. Synthesis of materials

Firstly, 1.0 g of cellulose and different milliliters of triethyl phosphate (0.1, 0.5, 1, 2 mL) (Fig. S1) were under stirring uniformly dissolved in 20 mL deionized water, respectively. After that, the mixed solutions were transferred into 25 mL Teflon reaction liners and heated at 200 $^{\circ}C$ for 12 h. After natural cooling, the mixed solutions were filtered by centrifugation, and sequentially washed with deionized water and ethanol. Eventually, the collected precipitates were dried overnight at 60 $^{\circ}C$ under vacuum, and the products were called P-HTCC (x mL P). In this article, P-HTCC stands for P-HTCC (1 mL P) if there is not marked.

Real raw agriculture waste is also applied. Dicranopteris dichotoma and straw were crushed to make them small fragments (Fig. S2). Then, 1.0 g of dicranopteris dichotoma was added to 20 mL of deionized water or the solution containing 1 mL triethyl phosphate. After stirring for half an hour, it was transferred to a 25 mL Teflon reaction liner and heated at 200 $^{\circ}C$ for 12 h. The following steps are the same as P-HTCC. The obtained products were called HTCC-DP and P-HTCC-DP. The transformation method of rice straw is the same as it, and the obtained products are called HTCC-RS and P-HTCC-RS.

2.3. Characterization

The morphology and microstructure images of the P-HTCC were characterized by scanning electronic microscopy (SEM, Sigma 500) and transmission electron microscope (TEM) equipped with energy dispersive X-ray spectra (EDS). The phase composition of the sample was examined by X-ray diffraction (XRD, Rigaku Ultima IV) using $Cu K\alpha$ source irradiation. Binding energy, chemical states of elements and compositions of P-HTCC were performed by X-ray photoelectron spectroscopy (XPS) spectrometer. UV-visible spectrophotometer (UV-Vis) was carried out to investigate the optical properties of P-HTCC, the wavelength range is 400–800 nm. Electron paramagnetic resonance (EPR, Bruker A300) tests were performed by using DMPO as a probe. Electro-catalysis measurements were acquired from a Model CHI760E workstation. The chemical structures were determined by solid state ^{13}C

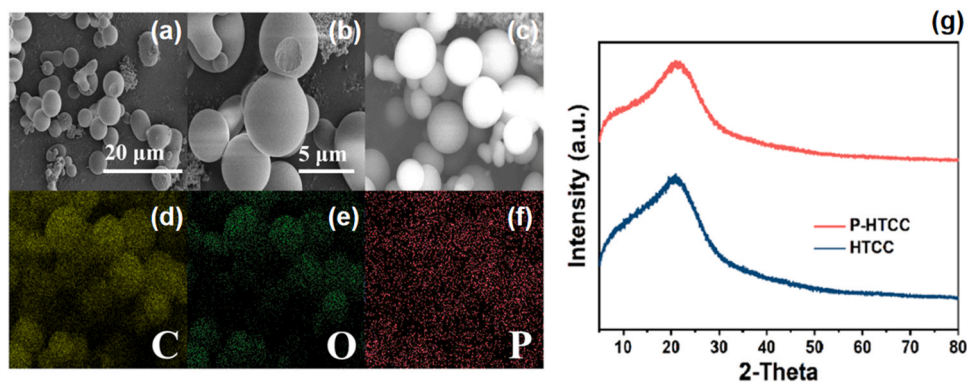


Fig. 1. (a, b) SEM images; (c-f) EDS spectra and EDS mapping; (g) XRD of P-HTCC and HTCC.

nuclear magnetic resonance spectroscopy (^{13}C NMR). The SEM, XRD, EPR, and UV-vis are from the School of Environmental Science and Engineering, Sun Yat-sen University.

2.4. Photocatalytic activity experiments

Photocatalytic H_2O_2 production experiments were conducted in pure water. Firstly, 10 mg P-HTCC was dispersed in 50 mL of deionized water. Then, the reaction was initiated under visible light irradiation using a PLS-FX300HU Xe lamp from Beijing Perfectlight Technology Co., Ltd with a cut-off filter ($\lambda \geq 420$ nm). The average light intensity was 10 mW cm^{-2} . At certain time intervals, 0.5 mL of the solution was sampled and filtered through a $0.22 \mu\text{m}$ Millipore filter to remove the photocatalyst for the detection of hydrogen peroxide concentration.

Meanwhile, degradation experiments were performed in an aqueous solution containing 2 ppm of ibuprofen (IBU). The amount of material

and reaction conditions are consistent with the above. At predetermined intervals, 1 mL of the reaction solution, then immediately added 2 mM Fe^{2+} to degrade 2 ppm IBU for 10 min. After the reaction, the concentration change of IBU before and after the reaction was detected by high performance liquid chromatography (HPLC) equipped with a UV detector and C18 column ($4.6 \text{ mm} \times 250 \text{ mm}$).

All photocatalytic reactions were performed under aeration unless otherwise stated. If any other atmospheres (O_2 or Ar) were used, O_2 or Ar should be bubbled into the suspension for no less than 30 min before the reaction, in all experiments, the gas flow rate was $1 \text{ L} \cdot \text{min}^{-1}$. The temperature was at 25°C .

2.5. Measurement of H_2O_2

The instantaneous concentration of H_2O_2 in the system was detected using the N, N-diethyl-1,4-phenylene-diamine (DPD) method. In detail,

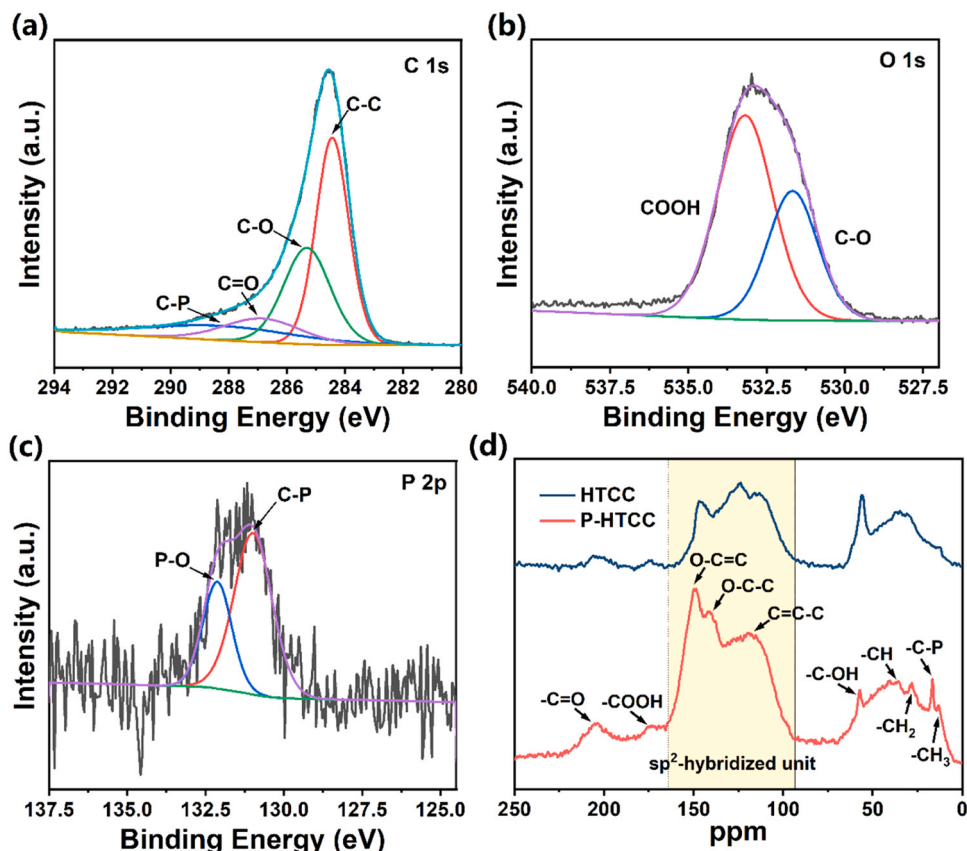


Fig. 2. High resolution XPS spectra of (a) C 1s, (b) O 1s and (c) P 2p, (d) ^{13}C solid-state NMR of P-HTCC.

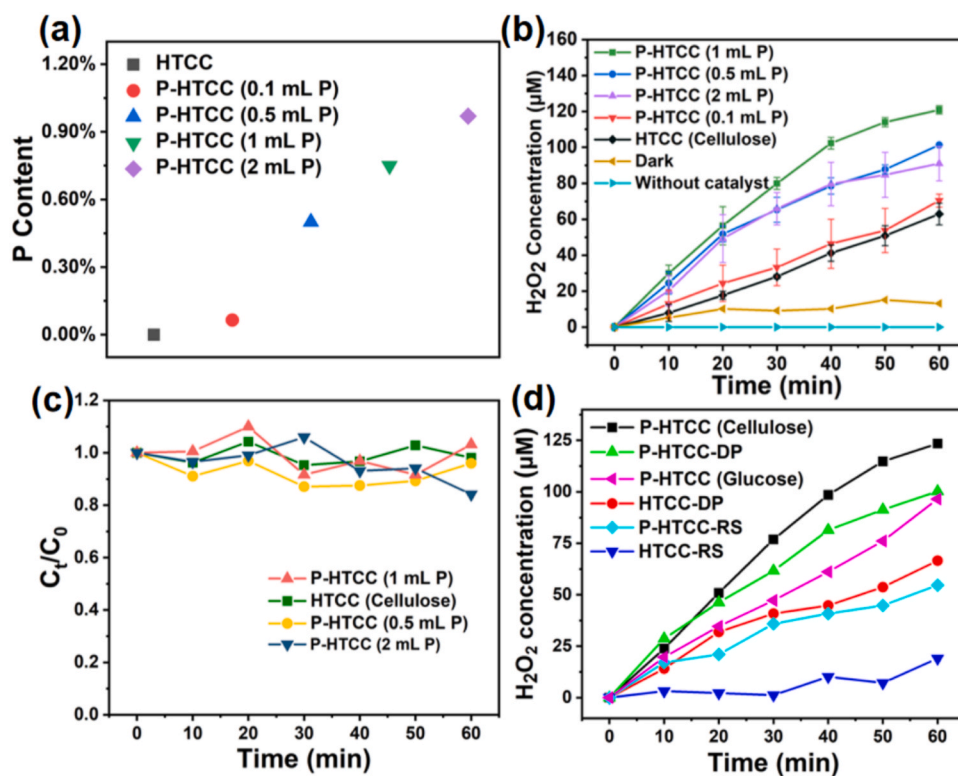


Fig. 3. (a) The loading of P in different catalysts, (b) Photocatalytic performance of different OP doping amount catalysts for H₂O₂ production and some important controls, (c) Reaction of different catalysts with H₂O₂, (d) H₂O₂ production by HTCC and P-HTCC from different biomass.

at given time intervals, 0.5 mL of the liquid sample was sampled and filtrated through 0.22 μm membranes. Then, 1.7 mL buffer solution (1 M phosphate, pH = 6) was mixed with 0.3 mL liquid sample, 0.05 mL of 1% DPD reagents and 0.05 mL horseradish peroxidase reagent. The reaction solution was measured at 552 nm by a UV-Vis spectrophotometer. A series of different concentrations of H₂O₂ samples were prepared to obtain the calibrated curve (Fig. S3). The detection limit was 1 μM.

2.6. Photoelectrochemical experiments

The photoelectrochemical properties of the materials were tested with a CHI760E electrochemical workstation. The photoelectrochemical experiments were measured with a three-electrode system (using an Ag/AgCl electrode and Pt wire electrode as reference and counter electrodes, respectively). The working electrode was prepared as follows: 10 mg of catalyst was dissolved in 300 μL of a solution containing 0.1 wt% Nafion, the mixture was sonicated for 30 min, and 50 μL of the suspension was taken and coated on the working electrode. In all experimental projects, the electrolyte was 0.5 M Na₂SO₄.

2.7. Theoretical calculations

The Vienna Ab initio simulation package (VASP) was used for all the calculations in this article [29,30]. We applied the projector-augmented-wave method with Perdew–Burke–Ernzerhof GGA functional [31,32]. The electronic convergence limit was set to be 1×10^{-4} eV. Optimization of atomic coordinates was considered to be converged if the Hellmann–Feynman force was smaller than 2×10^{-2} eV Å⁻¹. The slab of HTCC and P-HTCC were constructed. A series of intermediate like *O₂, *OOH, *H₂O₂ were constructed. The vacuum region was about 15 Å in height.

3. Results and discussion

3.1. Characterization

The morphology of P-HTCC and distribution of C, O and P elements in the material was characterized by using SEM and EDS mapping. As shown in Fig. 1a, b, P-HTCC is a microsphere of about 5 μm. Fig. 1c–f is the EDS mapping of the sample. It can be seen that the elements C, O and P are uniformly distributed on the microspheres, indicating that P is uniformly doped into the HTCC. The crystal structure of P-HTCC was detected by XRD. As shown in Fig. 1g, the relative intensities and peak positions of P-HTCC are not much different from those of pure HTCC. It might be because the P content is low, and the diffraction intensity of P is weak, so it can not be detected in the XRD pattern of P-HTCC.

The surface chemical and elemental states of P-HTCC were further examined using XPS technology. The high-resolution XPS spectra of C 1s, O 1s and P 2p for the P-HTCC composite are shown in Fig. 2a–c. The C 1s spectrum of the P-HTCC centered at 284.5 eV, 285.4 eV, 287.1 eV and 288.1 eV are attributed to C–C (carbon skeleton), C–O (combination of C and O), C=O (sp²-hybridized carbon), and C–P. The presence of hydroxyl and carboxyl groups are confirmed by O 1s spectrum. The signal can be divided into two peaks of 532.4 eV and 533.4 eV, which are the characteristic peaks of C–O and –COOH typical species, respectively. The P 2p peaks can be divided into two peaks of 130.9 eV and 132.3 eV, which correspond to P–C and P–O, respectively. The C 1s and P 2p of P-HTCC demonstrate the successful doping of P element to form C–P bonds in the C skeleton of HTCC.

The chemical structures of P-HTCC and pure HTCC were analyzed by ¹³C solid-state NMR. As shown in Fig. 2d, both P-HTCC and pure HTCC show O–C=C and C=C–C characteristic peaks belonging to furan rings at 149 ppm and 115–125 ppm. They are represented as polyfuran structures in the spectrum [33,34]. Meanwhile, the peaks at 205 ppm, 175 ppm and 57 ppm correspond to –C=O, –COOH and –C–OH groups, respectively. The characteristic C–H peaks of aliphatic compounds

Table 1
H₂O₂ photocatalytic yield reported in the literature.

Catalyst	H ₂ O ₂ yield (μmol·h ⁻¹ g ⁻¹)	References
FeOCl/CDots	112.4	[37]
PO ₄ ³⁻ coated Pd-BiVO ₄	60 (methanol as solvent)	[38]
α-Fe ₂ O ₃ /g-C ₃ N ₄	12	[39]
P doped g-C ₃ N ₄	174	[25]
K ⁺ doped g-C ₃ N ₄ /WO ₃	332.5	[40]

appeared at 40 ppm. It is worth noting that P-HTCC has a characteristic peak of C-P at 15 ppm, which indicates that the P-HTCC material successfully doped P into the HTCC structure, which is consistent with the XPS results.

3.2. Photocatalytic performance for H₂O₂ generation

Photocatalytic experiments were carried out by dispersing 0.2 g·L⁻¹ catalysts in deionized water under visible light irradiation and aeration conditions. We have observed the OP doping amount on the concentration of H₂O₂ production. As shown in Fig. 3b, when 0.1 mL OP was added, the performance of P-HTCC was basically the same as that of HTCC. This might be because the content of P loaded on the material was too small, and it didn't cause much change. However, when the OP increased to 0.5 mL or more, the performance of P-HTCC changed significantly. When the doping amount of OP was about 1 mL, the photocatalytic activity of P-HTCC reached the maximum value and the production of H₂O₂ was 920 μmol·h⁻¹ g⁻¹. However, further increasing the amount of OP doping leads to a decrease in the photocatalytic activity of P-HTCC. This is because when P is sufficient, it can promote the production of H₂O₂ in HTCC, but too much P doping in HTCC will act as a recombination center for electron-hole pairs, inhibiting the separation of photogenerated carriers, resulting in a decrease in the production of H₂O₂ [35].

Since we have changed the dosage of OP, the actual content of P in the material is an important factor that must be investigated. Here, the

actual doping amount of P in P-HTCC prepared by adding different contents of OP was measured by the potassium persulfate digestion method shown in S1 [36], and the calibrated curve is shown in Fig. S4. As shown in Fig. 3a, with the addition of different contents of OP, the content of the P element in the synthesized material was also different. When 0.1 mL OP was added, the content of P in the material was only 0.03297 mg·L⁻¹ (0.065% of the total weight of the material). When 0.5 mL, 1 mL and 2 mL OP were added, the content of P gradually increased to 0.25417, 0.3719 and 0.48607 mg·L⁻¹, respectively. This corresponds to 0.5%, 0.75%, 0.97% of the total weight of the material, respectively. Among them, the proportion of P element in 1 mL P-HTCC is basically consistent with the data in the XPS result (Table S1).

We have added some necessary control experiments to confirm the reliability of the experiment. The results are shown in Fig. 3b, as we expected, the material showed almost no H₂O₂ production performance without light or without catalyst. This indicates the importance of light and catalysts.

The total production of H₂O₂ produced in situ is also affected by the decomposition rate. It has been reported that P can cause the reductive decomposition of H₂O₂, thereby limiting its accumulation [35]. Therefore, we conducted comparative experiments by reacting materials with different P contents with H₂O₂. Fig. 3c shows that the P-HTCC synthesized by the hydrothermal process will not decompose H₂O₂ regardless of the amount of P doping, which indicates that the synthesized P-HTCC basically does not cause the decomposition of H₂O₂.

In addition to the effect of phosphorus, we also investigate the effect of different biomass sources on the production of H₂O₂ from the catalyst. As shown in Fig. 3d, the H₂O₂ photocatalytic synthesis performance of P-HTCC synthesized from cellulose is better than that of glucose, and compared with the H₂O₂ yield of photocatalysts reported in Table 1, P-HTCC also exhibits better performance. In addition to glucose, we have tried to combine a common plant, dicranopteris dichotoma, and a common agricultural by-product, rice straw, with OP to prepare P-HTCC-DP and P-HTCC-RS using the same method as cellulose. Their performance of H₂O₂ production under light and aerobic conditions was

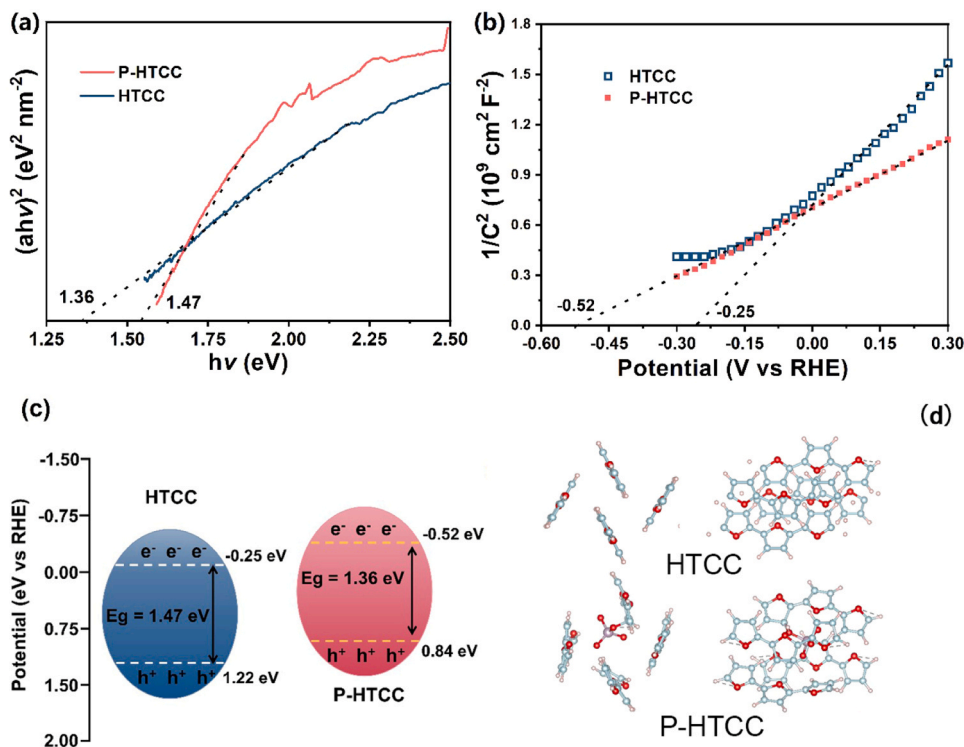


Fig. 4. (a) The flat band potential estimated by Mott-Schottky plot, (b) The bandgap estimated by Kubelka-Munk method, (c) Band structure of the P-HTCC. (d) Structure of HTCC and P-HTCC.

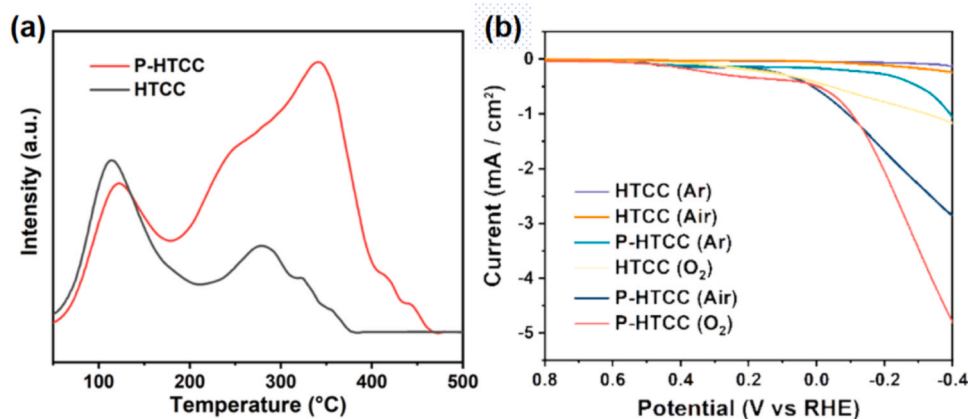


Fig. 5. (a) TPD-O₂, (b) CV curves of P-HTCC and HTCC under different conditions.

also compared in Fig. 3d. In the absence of organic P, the H₂O₂ yield of HTCC-DP at 60 min was about 67 μM , which was similar to the yield of pure HTCC. However, in the presence of OP, the yield of H₂O₂ increased to 101.25 μM at 60 min, which is 50% higher than the sample without OP. HTCC-RS converted from rice straw in the presence of OP also exhibits higher activity than that in the absence of OP. This shows that our experimental results are applicable to actual plants and crops, and have great application value.

To study the photoconversion efficiency in the system, we performed a calculation of the solar chemical conversion (SCC) efficiency. The calculation Eq. (1) is as follows:

$$\text{SCC}(\%) = \frac{\Delta G_{\text{H}_2\text{O}_2} (J \cdot \text{mol}^{-1}) \times n_{\text{H}_2\text{O}_2} (\text{mol})}{P (W \cdot \text{m}^{-2}) \times A (\text{m}^2) \times t (\text{s})} \quad (1)$$

Where, $\Delta G_{\text{H}_2\text{O}_2}$ is the free energy of generating H₂O₂, which is 117 $\text{kJ} \cdot \text{mol}^{-1}$, $n_{\text{H}_2\text{O}_2}$ is the mole amount of H₂O₂ generated in the reaction system, and P is the light intensity of the simulated solar light source, A is the illumination area, and t is the reaction time.

In the actual study, the irradiance of the simulated solar source is 10 $\text{mW} \cdot \text{cm}^{-2}$, and the irradiation area is 19.635 cm^2 . The reaction time was 1 h, the amount of H₂O₂ produced by 10 mg P-HTCC in 50 mL solution was 123 $\mu\text{mol} \cdot \text{L}^{-1}$, and the amount of H₂O₂ produced by 10 mg HTCC in 50 mL solution was 62 $\mu\text{mol} \cdot \text{L}^{-1}$. To sum up, according to Eq. (1), the SCC efficiencies of P-HTCC and HTCC can be calculated to be 0.1% and 0.05%, respectively, which shows that P-HTCC can use sunlight more effectively to achieve higher O₂ reduction efficiency.

3.3. P-HTCC band structure

According to energy band theory, molecular oxygen activation can only be achieved when the conduction band (CB) potential of the semiconductor is lower than the standard redox potential of O₂/•O₂ (E = −0.046 eV vs. NHE). Theoretically, the more negative the CB, the more likely the molecular oxygen will be activated. Generally, electron-donating ion doping (n-type doping) will increase the Fermi level of the semiconductor and move the CB position, which can effectively promote the activation of molecular oxygen and the generation of ROS. In addition, a new doping energy level is formed between the CB and valence band (VB) of the semiconductor after doping, which reduces the efficiency of carrier recombination, thereby enhancing the activation of molecular oxygen.

The band structures of the as-prepared P-HTCC and HTCC were determined through a series of experiments. As shown in Fig. 4a, from the Kubelka–Munk diagram obtained by transforming the UV-Vis diffuse reflection absorption spectrum by the Tauc method, the band gaps of P-HTCC and HTCC were calculated to be 1.36 eV and 1.47 eV. In addition, Mott-Schottky (MS) plots were used to analyze the band structure of the

material (Fig. 4b). The MS curves of P-HTCC and HTCC show a linear increase with the increase of bias voltage, indicating that the materials are all typical n-type semiconductors, and the slope of HTCC is greater than that of P-HTCC, so the number of carriers of P-HTCC is greater than that of HTCC. The high carrier separation efficiency is beneficial to the electron transfer process activated by molecular oxygen.

At the same time, the flat-band potentials of P-HTCC and HTCC can be determined to be −0.52 V vs. RHE and −0.25 V vs. RHE, respectively, based on the x-intercepts of the MS curves. It is well known that in typical n-type semiconductors, the flat-band potential is close to the Fermi level. Therefore, the CB of P-HTCC is −0.52 V vs. RHE, and the CB of HTCC is −0.25 V vs. RHE. In summary, the band structures of P-HTCC and HTCC are shown in Fig. 4c, and the difference in the band structures of P-HTCC and HTCC is attributed to the influence of P in its formation.

The formation energy of P-HTCC is calculated by the following equation:

$$E_f = E_{\text{tot}} - E_{\text{HTCC}} - E_{\text{PO}_4} \quad (2)$$

Where E_{ad} is the adsorption energy, E_{tot} is the total energy, E_{HTCC} is the energy of the HTCC substrate and E_{PO_4} is the energy of the PO₄³⁺ molecule. The calculated energy is −5.15 eV, suggesting the formation of P-HTCC is thermodynamically favorable.

Interestingly, the insertion of the PO₄³⁺ molecule induces the twist of the polyfuran chains of the HTCC. Compared with pure HTCC containing regular polyfuran chains, the P-HTCC is composed of disturbed polyfuran chains. This twist optimizes the electronic structure of the HTCC. The partial density of states (PDOS) of P-HTCC is shown in Figs. S5, S6. With the addition of the P element, the PDOS are not as regular as those without P. Also, it is found that the PDOS of P element lies below the VB band. Both the VB and CB bands are composed of C and O electrons. This means that the P element only changes the structure of the HTCC and its electrons do not directly contribute to the photocatalysis process.

3.4. Photocatalytic mechanism

3.4.1. Oxygen adsorption of P-HTCC

It is well known that the O₂ adsorption capacity of materials is a key parameter for the catalytic activity of the oxygen reduction reaction [41]. The introduction of P atoms into carbon-based materials will reduce the adsorption energy of O₂, and favorable O₂ adsorption promotes the activation of O₂, which is of positive significance for the generation of H₂O₂. Here, the effects of P-HTCC and HTCC on O₂ adsorption capacity were verified by TPD-O₂ results. As shown in Fig. 5a, both P-HTCC and HTCC have obvious desorbed oxygen signals below 100 °C, which is attributed to the desorption of physically adsorbed O₂. The oxygen desorption peaks starting to be released near

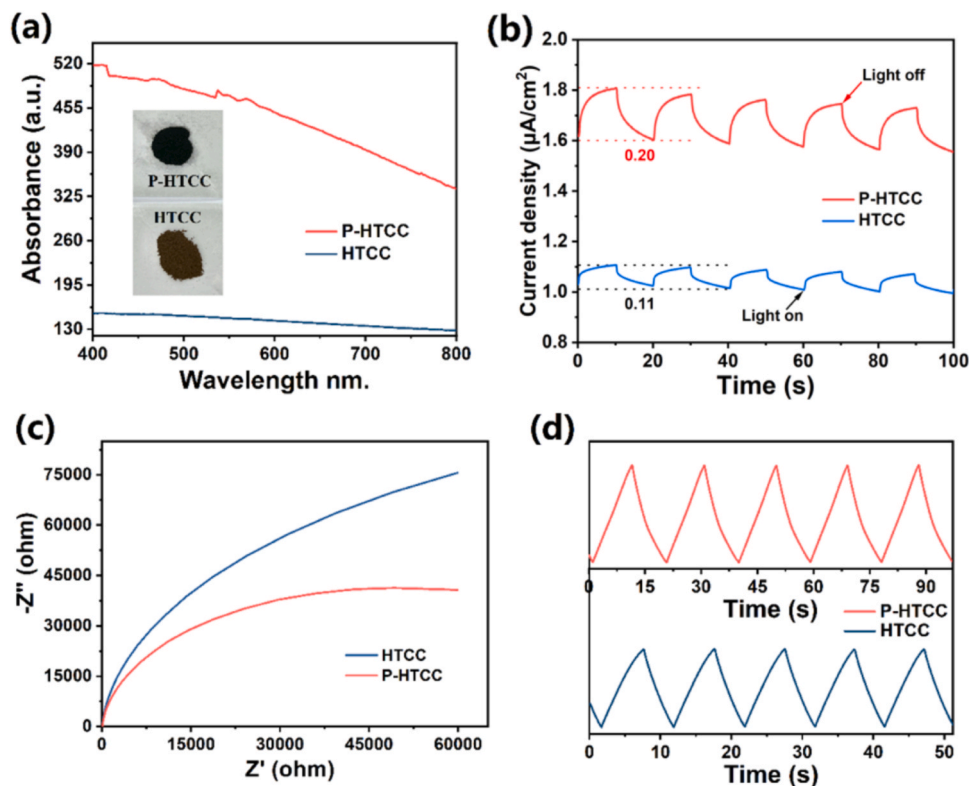


Fig. 6. (a) UV-vis DRS, (b) photocurrent measurement, (c) EIS, (d) Galvanostatic measurement of P-HTCC and HTCC.

300 °C are derived from chemisorption [42]. For this peak, the adsorption capacity of the material for oxygen increased greatly from 1.76 $\text{mmol}\cdot\text{g}^{-1}$ of HTCC to 3.41 $\text{mmol}\cdot\text{g}^{-1}$ of P-HTCC, which was almost twice that of the former, indicating that the introduction of P element greatly enhanced the adsorption capacity of P-HTCC for oxygen.

Afterwards, cyclic voltammetric (CV) curves were used in the voltage range -0.4 V to 0.8 V to compare the oxygen reduction reaction (ORR) performance of the as-prepared materials under different atmospheric conditions. As shown in Fig. 5b, compared with HTCC, the ORR current of P-HTCC is significantly stronger than that of HTCC at a potential of -0.4 V, which also indicates that P-HTCC improves the photocatalytic performance. At the same time, under different atmospheric conditions, the reduction current intensity of the samples is different, the CV curve of P-HTCC under Ar condition is relatively small, and a small ORR peak can be observed at -0.4 V. In contrast, under air conditions, especially under O_2 conditions, the current density is significantly increased, with a current intensity as high as $-4.8 \text{ mA}\cdot\text{cm}^{-2}$. This suggests that ORR on P-HTCC occurs only under oxygen-containing conditions with good oxygen uptake and reduction.

3.4.2. Photoelectrochemical performance of P-HTCC

The optical absorption characteristics of P-HTCC and HTCC were analyzed with UV-Vis DRS. As shown in Fig. 6a, the spectral absorption result of HTCC shows its semiconductor properties, while the spectral absorption of P-HTCC maintains high absorption intensity in the range of 400–800 nm, which is mainly due to the reduced electronic band gap of P-HTCC. At the same time, it can be seen from the inset that the color of the P-HTCC sample changes from tan to dark black, which also makes the absorption intensity of P-HTCC stronger. Therefore, P-HTCC is composed of a light-absorbing framework and a semiconducting sp^2 hybrid structure, which can generate photoexcited electrons and holes under illumination.

The photoresponse properties of P-HTCC and HTCC were measured by the transient photocurrent (STEP) curves at open circuit potential. As shown in Fig. 6b, the response intensity of HTCC to visible light is very

small ($0.11 \mu\text{A}\cdot\text{cm}^{-2}$), while the photocurrent intensity of P-HTCC under illumination is $0.20 \mu\text{A}\cdot\text{cm}^{-2}$, much higher than that of HTCC. This indicates that the doping P can not only enhance the photoresponse current intensity, but also increase the transient photocurrent intensity, which is conducive to the rapid separation of photogenerated charges, and also corresponds to higher photocatalytic activity.

Electrochemical impedance spectroscopy (EIS) further confirmed the better interfacial charge transfer properties in P-HTCC. It can be seen from Fig. 6c that the radius of the semicircular Nyquist curve of P-HTCC is smaller than that of HTCC, indicating that P-HTCC has lower charge transfer resistance and faster interface charge transfer speed, which is beneficial to the electrons transfer process. With the improved charge separation efficiency, O_2 can be highly converted to H_2O_2 on the CB of P-HTCC.

The larger the electrochemically active surface area means, the more reactive sites there are, and the better the catalytic performance. The electrochemically active surface areas of P-HTCC and HTCC were evaluated by their capacitance according to galvanostatic measurements. In capacitance measurement experiments, a constant current of 5 to $-5 \mu\text{A}$ was intermittently applied across the material. The specific capacitance C can be estimated according to the Eq. (3) charge/discharge curve:

$$C = \frac{I \times \Delta t}{\Delta V} \quad (3)$$

Among them, I is the current density during the charging and discharging process, Δt is the charging and discharging duration of each segment, and ΔV is the potential difference. In the experiment, since I and ΔV are regarded as constants, the specific capacitance is proportional to Δt . Fig. 6d shows that the Δt of P-HTCC is greater than that of HTCC, and the ratio between the two is 1.9, which means that the electrochemically active surface area of P-HTCC becomes larger.

3.4.3. Photocatalytic oxygen reduction to H_2O_2 mechanism

Firstly, the role of oxygen, and the production of H_2O_2 in different atmospheres were studied. When argon inert gas was introduced into the

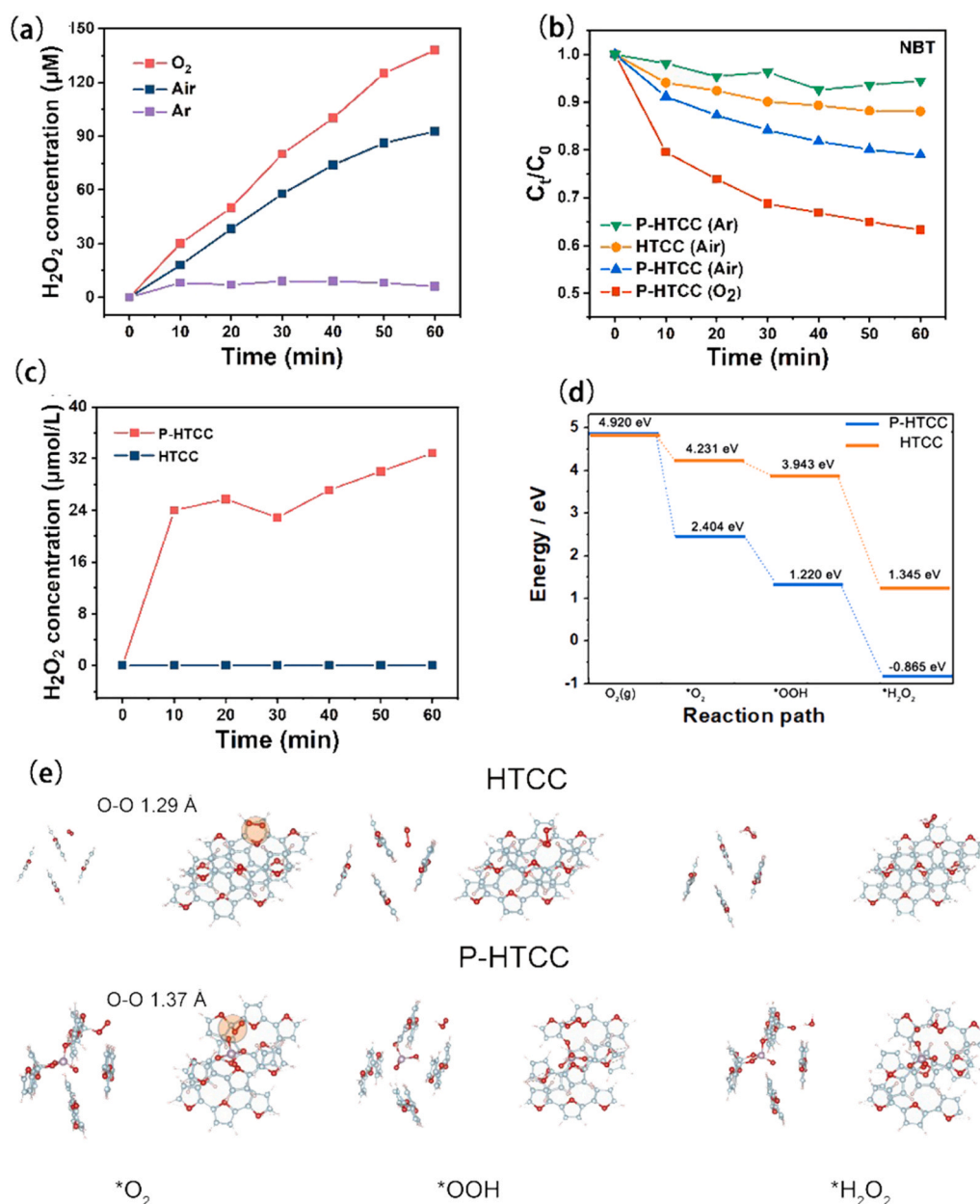
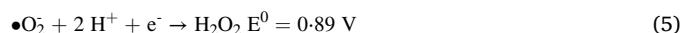


Fig. 7. (a) Photocatalytic performance for H₂O₂ production under different conditions, (b) NBT removal under different conditions, (c) NBT on the inhibition performance, (d) Energy diagram for the generation of H₂O₂ on HTCC and P-HTCC, (e) Structure of HTCC and P-HTCC adsorbing *O₂, *OOH and *H₂O₂.

reaction system instead of oxygen during the photocatalytic process, if no H₂O₂ was produced, it indicated that H₂O₂ was mainly produced through the activation process of molecular oxygen. We have carried out comparative experiments of photocatalytic production of H₂O₂ under different atmospheric conditions. The results are shown in Fig. 7a. Under different atmospheric conditions, the performance of the photocatalytic production of H₂O₂ is different. Under the condition of argon, almost no H₂O₂ is produced, while under the air condition, the yield of H₂O₂ is 617 μmol·h⁻¹ g⁻¹, and when under the condition of O₂, the yield is significantly improved to 920 μmol·h⁻¹ g⁻¹. These results indicate that oxygen is involved in the photocatalytic H₂O₂ production process of P-HTCC, and the H₂O₂ production is through the reduction of oxygen.

Then, a two-step one-electron transfer process or a one-step two-electron process for oxygen reduction was studied. In fact, there are two ways for oxygen reduction to H₂O₂. They are two step one-electron process (O₂ to •O₂ to H₂O₂) and the one step two-electron transfer process (O₂ to H₂O₂ directly).



As shown in Eqs. (4) and (5), in the process of two step one-electron process, the one-electron reduction reaction of oxygen occurs is the first step, and the electrons on the conduction band of the material and the oxygen molecules adsorbed on the surface undergo a single-electron reduction reaction. Electron transfer reaction to generate •O₂. Afterwards •O₂ can undergo electron reduction and hydrogenation to form H₂O₂.



In the one step two-electron transfer process, oxygen is adsorbed on the surface of the material to obtain two electrons, and combined with H⁺ to directly generate H₂O₂ as shown in Eq. (6). There is no superoxide radical in the system.

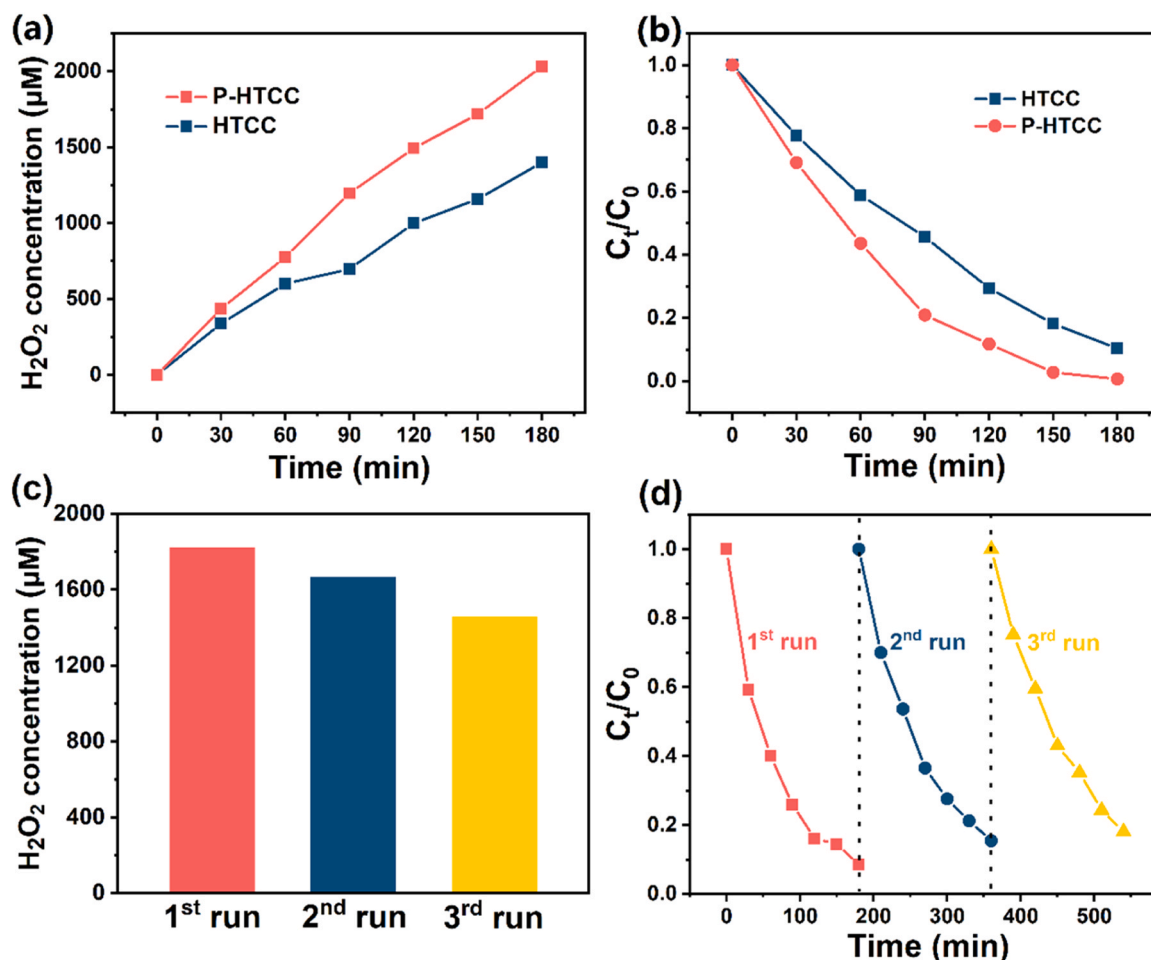
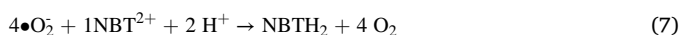


Fig. 8. Photocatalytic performance for (a) H₂O₂ production and (b) IBU degradation, Recycling tests for (c) H₂O₂ production and (d) IBU degradation.

A NBT trap is used to distinguish the path of oxygen reduction to H₂O₂. This is because NBT can react with •O₂ in a molar ratio of 1:4 to convert to Eq. (7), and the amount of •O₂ is calculated by monitoring the intensity of the maximum absorbance of NBT at 259 nm [43].



If the absorbance of NBT decreases with the increase of reaction time, and no H₂O₂ is generated after adding the collector NBT, it means that H₂O₂ is only generated by the single electron transfer process of molecular oxygen. Otherwise, when the generation of H₂O₂, is only partially inhibited, both two-electron transfer paths and single-electron transfer paths exist.

The results are shown in Fig. 7b. After adding the trapping agent NBT, the NBT content in the solution decreased, indicating that •O₂ did exist in the system. Especially when oxygen was introduced into the reaction solution, the NBT content decreased much more than that of argon, which indicates that there is a single electron transfer process in the production of H₂O₂. According to formulas 4, 5, and 7, it was calculated that the P-HTCC system produced 14.7 μmol·L⁻¹ of •O₂ under the condition of oxygen ventilation, and the amount of •O₂ produced under the condition of air exposure (8.4 μmol·L⁻¹) is also much larger than that produced by HTCC in air (4.8 μmol·L⁻¹), which also indicates that the photocatalytic performance of P-HTCC is better than that of HTCC. Further qualitative evaluation of superoxide radicals was performed by electron paramagnetic resonance spectroscopy (EPR), DMPO is used as a spin trapping agent for superoxide radical and methanol is used as the reaction solution. As shown in Fig. S7, as we expected, the six-peak signal of DMPO-•O₂ with isotropic hyperfine appears on the

EPR spectrum [44], and the characteristic signal is stronger with the increase of reaction time, which confirms the production of •O₂.

As shown in Fig. 7c, when excess NBT was added to the P-HTCC reaction system, a small amount of H₂O₂ was still generated, but no H₂O₂ was detected by HTCC. This indicates that the process of H₂O₂ production by P-HTCC should be dominated by a single electron transfer pathway, and single electron transfer and double electron transfer processes coexist. By contrast, HTCC is a single electron transfer process.

3.4.4. Density functional calculation

We further use density functional calculation to explore the enhancement mechanism for activation process of O₂ on P-HTCC (Figs. S8-S10, Fig. 7e). The adsorption energy of O₂ is calculated by the following equation:

$$E_{\text{ad}} = E_{\text{tot}} - E_{\text{HTCC}} - E_{\text{O}_2} \quad (8)$$

Where E_{ad} is the adsorption energy, E_{tot} is the total energy, E_{HTCC} is the energy of the HTCC substrate and E_{O_2} is the energy of the O₂ molecule. The E_{ad} of HTCC is -0.689 eV and that of P-HTCC is -2.516 eV. The larger value of E_{ad} for P-HTCC indicates that the O₂ is easier to be activated. This is consistent with the experimental results of TPD-O₂. The O-O bond increases from 1.21 Å to 1.29 Å on pure HTCC, while it increases remarkably to 1.37 Å on P-HTCC, which strongly demonstrates the advantage of P-HTCC.

Subsequently, the activation of O₂ to H₂O₂ usually follows the process of *O₂*+•OOH*+H₂O₂. Here, we calculated the change of Gibbs free energy. Firstly, the adsorption of the O₂ molecule is much easier on P-HTCC than HTCC and the change of Gibbs free energy decreases more

obviously on P-HTCC than HTCC. Then, in the step of $\cdot\text{OOH}$, the energy is 3.943 eV on HTCC, while decreases to 1.220 eV on P-HTCC. Finally, in the step of H_2O_2 , the energy is 1.345 eV on HTCC, while decreases to -0.865 eV on P-HTCC. This energy change demonstrates that: 1) Both HTCC and P-HTCC are beneficial to the generation of H_2O_2 . 2) It is easier for the generation of H_2O_2 on P-HTCC than HTCC.

3.5. Photocatalytic degradation and stability of P-HTCC

In addition to the research on the photocatalytic mechanism of P-HTCC materials, the degradation experiments of organic pollutants were also carried out by utilizing their H_2O_2 producing properties. For the photocatalytic experiment solution, 1 mL of sample solution was taken at certain time intervals, and 2 mM Fe^{2+} was added to the 2 ppm IBU solution for 10 min. The IBU concentration in each stage of the catalytic reaction was then determined by HPLC. The results are shown in Fig. 8a, b, HTCC can generate enough H_2O_2 to degrade IBU, and 90% of IBU was eliminated within 3 h. The incorporation of P significantly enhanced the photocatalytic activity of HTCC. P-HTCC produced up to 2 mM H_2O_2 within 3 h, and the Fenton reaction with Fe^{2+} produced $\cdot\text{OH}$ active species that could completely degrade IBU. The enhanced photocatalytic activity may be due to the more negative conduction band, which is conducive to efficient electron-hole pair separation.

To evaluate the photocatalytic stability of P-HTCC, the catalyst was separated and recovered from the reaction solution by centrifugal filtration, washed and dried, and then repeated for three consecutive photocatalytic cycles. As shown in Fig. 8c, d, the photocatalytic H_2O_2 production of P-HTCC remained basically stable after three cycle experiments, and the H_2O_2 production after the third cycle experiment was 80% of the first cycle experiment. Meanwhile, the system exhibited excellent IBU degradation efficiency within 180 min, even after three cycles.

4. Conclusion

Here, we provide a method for treating organophosphorus pollutants and biomass waste, which is convert them into P-HTCC photocatalysts by a simple hydrothermal method. Under the condition of O_2 and illumination, efficient synthesis of H_2O_2 was achieved. P-HTCC photocatalytically reduces O_2 in pure water without any sacrificial agent, and the H_2O_2 yield is as high as $920 \mu\text{mol} \cdot \text{h}^{-1} \text{g}^{-1}$, which is double that of pure HTCC. Through a series of experimental studies and calculations, the doping of P changes the energy band structure of HTCC, makes the conduction band more negative, and improves the absorption capacity of visible light and O_2 , which is conducive to the effective separation of electron-hole pairs. What's more, the H_2O_2 produced in the process can effectively treat organic pollutants in situ.

CRedit authorship contribution statement

Hu Zhuofeng: Formal analysis, Resources, Software, Supervision, Writing – original draft, Writing – review & editing. **He Xi:** Data curation, Formal analysis. **Li Lejing:** Data curation, Formal analysis. **Yu Jimmy C.:** Conceptualization, Formal analysis, Supervision. **Cai Junjie:** Conceptualization, Data curation, Formal analysis, Supervision. **Wang Xiaoli:** Data curation. **Ou Zhesun:** Data curation. **Sun Mengdi:** Data curation. **Yue Xin:** Data curation. **Luo Guanghui:** Data curation. **Liu Huimin:** Data curation. **Lu Yinglong:** Data curation, Formal analysis, Writing – review & editing. **Zhou Quan:** Conceptualization. **Wang Ruilin:** Data curation. **Duan Chengyu:** Data curation.

Declaration of Competing Interest

The authors declare that they have no known competing financial interests or personal relationships that could have appeared to influence the work reported in this paper.

Data availability

No data was used for the research described in the article.

Acknowledgments

This work is supported by the Guangzhou Basic and Applied Basic Research Foundation, China (202201011695), the National Natural Science Foundation of China, China (Grant No. 51902357); the Natural Science Foundation of Guangdong Province, China (2019A1515012143); the Fundamental Research Funds for the Central Universities, Sun Yat-sen University, China (22lgqb23); the Guangdong Basic and Applied Basic Research Foundation, China (2019B1515120058). The theoretical calculation is supported by National supercomputer center in Guangzhou and National supercomputing center in Shenzhen (Shenzhen cloud computing center).

Appendix A. Supporting information

Supplementary data associated with this article can be found in the online version at doi:10.1016/j.apcatb.2024.123771.

References

- [1] S. Yuan, C. Li, H. Yu, Y. Xie, Y. Guo, W. Yao, Selective uptake determines the variation in degradation of organophosphorus pesticides by *Lactobacillus plantarum*, *Food Chem.* 360 (2021) 130106–130114, <https://doi.org/10.1016/j.foodchem.2021.130106>.
- [2] S.N. Sinha, M. Vishnu Vardhana Rao, K. Vasudev, M. Odetokun, A liquid chromatography mass spectrometry-based method to measure organophosphorus insecticide, herbicide and non-organophosphorus pesticide in grape and apple samples, *Food Control* 25 (2012) 636–646, <https://doi.org/10.1016/j.foodcont.2011.11.031>.
- [3] T. Reemtsma, J.B. Quintana, R. Rodil, M. García-López, I. Rodríguez, Organophosphorus flame retardants and plasticizers in water and air I. Occurrence and fate, *TrAC Trends Anal. Chem.* 27 (2008) 727–737, <https://doi.org/10.1016/j.trac.2008.07.002>.
- [4] S.H. Brandsma, J. de Boer, P.E.G. Leonards, W.P. Cofino, A. Covaci, P.E. G. Leonards, Organophosphorus flame-retardant and plasticizer analysis, including recommendations from the first worldwide interlaboratory study, *TrAC Trends Anal. Chem.* 43 (2013) 217–228, <https://doi.org/10.1016/j.trac.2012.12.004>.
- [5] K. Xiao, N. Zhu, Z. Lu, H. Zheng, C. Cui, Y. Gao, Y. Gao, X. Meng, Y. Liu, M. Cai, Distribution of eight organophosphorus pesticides and their oxides in surface water of the East China Sea based on high volume solid phase extraction method, *Environ. Pollut.* 279 (2021) 116886–116893, <https://doi.org/10.1016/j.envpol.2021.116886>.
- [6] J. He, Z. Wang, L. Zhao, H. Ma, J. Huang, H. Li, X. Mao, T. Huang, H. Gao, J. Ma, Gridded emission inventory of organophosphorus flame retardants in China and inventory validation, *Environ. Pollut.* 290 (2021) 118071–118078, <https://doi.org/10.1016/j.envpol.2021.118071>.
- [7] X. Gao, Y. Lin, J. Li, Y. Xu, Z. Qian, W. Lin, Spatial pattern analysis reveals multiple sources of organophosphorus flame retardants in coastal waters, *J. Hazard Mater.* 417 (2021) 125882–125890, <https://doi.org/10.1016/j.jhazmat.2021.125882>.
- [8] U.E. Bollmann, A. Möller, Z. Xie, R. Ebinghaus, J.W. Einax, Occurrence and fate of organophosphorus flame retardants and plasticizers in coastal and marine surface waters, *Water Res.* 46 (2012) 531–538, <https://doi.org/10.1016/j.watres.2011.11.028>.
- [9] J. Ahlgren, L. Tranvik, A. Gogoll, M. Waldeback, K. Markides, E. Rydin, Sediment depth attenuation of biogenic phosphorus compounds measured by ^{31}P NMR, *Environ. Sci. Technol.* 39 (2005) 867–872, <https://doi.org/10.1021/es049590h>.
- [10] L. Xu, Y. Liu, Z. Hu, J.C. Yu, Converting cellulose waste into a high-efficiency photocatalyst for Cr(VI) reduction via molecular oxygen activation, *Appl. Catal. B-Environ.* 295 (2021), <https://doi.org/10.1016/j.apcatb.2021.120253>.
- [11] Z. Hu, Z. Shen, J.C. Yu, Converting Carbohydrates to Carbon-Based Photocatalysts for Environmental Treatment, *Environ. Sci. Technol.* 51 (2017) 7076–7083, <https://doi.org/10.1021/acs.est.7b00118>.
- [12] Y. Peng, X. He, N. Zheng, R. Hu, W. Guo, Z. Hu, Transferring waste of biomass and heavy metal into photocatalysts for hydrogen peroxide activation, *Chem. Eng. J.* 420 (2021), <https://doi.org/10.1016/j.cej.2021.129867>.
- [13] Z. Hu, Y. Huang, X. He, W. Guo, K. Yan, Solution-phase conversion of glucose into semiconductive carbonaceous nanosheet photocatalysts for enhanced environmental applications, *Chem. Eng. J.* 427 (2022), <https://doi.org/10.1016/j.cej.2021.131464>.
- [14] Z. Hu, G. Liu, X. Chen, Z. Shen, J.C. Yu, Enhancing Charge Separation in Metallic Photocatalysts: A Case Study of the Conducting Molybdenum Dioxide, *Adv. Funct. Mater.* 26 (2016) 4445–4455, <https://doi.org/10.1002/adfm.201600239>.
- [15] L. Xu, Y. Liu, Z. Hu, J.C. Yu, Converting cellulose waste into a high-efficiency photocatalyst for Cr(VI) reduction via molecular oxygen activation, 120253-

- 120163, *Appl. Catal. B: Environ.* 295 (2021), <https://doi.org/10.1016/j.apcatb.2021.120253>.
- [16] H. Hou, X. Zeng, X. Zhang, Production of Hydrogen Peroxide by Photocatalytic Processes, *Angew. Chem. Int. Ed.* 59 (2020) 17356–17376, <https://doi.org/10.1002/anie.201911609>.
- [17] Z.G. Li, C.W. Wang, A. Kumar, H.R. Jia, Y. Jia, H.F. Li, L. Bai, G.X. Zhang, X.M. Sun, Anisotropic solution growth of 1D/2D N-rich carbon, *Adv. Powder Mater.* 2 (2023), <https://doi.org/10.1016/j.apmate.2023.100138>.
- [18] S. Lin, N. Zhang, F. Wang, J. Lei, L. Zhou, Y. Liu, J. Zhang, Carbon Vacancy Mediated Incorporation of Ti3C2 Quantum Dots in a 3D Inverse Opal g-C3N4 Schottky Junction Catalyst for Photocatalytic H2O2 Production, *ACS Sustain. Chem. Eng.* 9 (2020) 481–488, <https://doi.org/10.1021/acssuschemeng.0c07753>.
- [19] Y. Yang, Y. Tang, H. Jiang, Y. Chen, P. Wan, M. Fan, R. Zhang, S. Ullah, L. Pan, J.-J. Zou, M. Lao, W. Sun, C. Yang, G. Zheng, Q. Peng, T. Wang, Y. Luo, X. Sun, A. S. Konev, O.V. Levin, P. Lianos, Z. Hu, Z. Shen, Q. Zhao, Y. Wang, N. Todorova, C. Trapalis, M.V. Sheridan, H. Wang, L. Zhang, S. Sun, W. Wang, J. Ma, 2020 Roadmap on gas-involved photo- and electro- catalysis, *Chin. Chem. Lett.* 30 (2019) 2089–2109, <https://doi.org/10.1016/j.cclet.2019.10.041>.
- [20] C. Chu, Q. Zhu, Z. Pan, S. Gupta, D. Huang, Y. Du, S. Weon, Y. Wu, C. Muehich, E. Stavitski, K. Domen, J.H. Kim, Spatially separating redox centers on 2D carbon nitride with cobalt single atom for photocatalytic H2O2 production, *Proc. Natl. Acad. Sci. USA* 117 (2020) 6376–6382, <https://doi.org/10.1073/pnas.1913403117>.
- [21] H. Xie, Y. Zheng, X. Guo, Y. Liu, Z. Zhang, J. Zhao, W. Zhang, Y. Wang, Y. Huang, Rapid Microwave Synthesis of Mesoporous Oxygen-Doped g-C3N4 with Carbon Vacancies for Efficient Photocatalytic H2O2 Production, *ACS Sustain. Chem. Eng.* 9 (2021) 6788–6798, <https://doi.org/10.1021/acssuschemeng.1c01012>.
- [22] Y. Wang, Y. Wang, J. Zhao, Y. Xu, Effect of inorganic ions on H2O2 production over illuminated Au/WO3 with visible light, *Appl. Catal. B: Environ.* 299 (2021), <https://doi.org/10.1016/j.apcatb.2021.120676>.
- [23] N. Liu, Y. Liu, Y. Liu, Y. Li, Y. Cheng, H. Li, Modulation of photogenerated holes for enhanced photoelectrocatalytic performance, *Microstructures* 1 (2023) 2023001, <https://doi.org/10.20517/microstructures.2022.23>.
- [24] J. Xu, Q. Ji, Y. Wang, C. Wang, L. Wang, Enhanced photocatalytic H2/H2O2 production and tetracycline degradation performance of CdSe quantum dots supported on K, P, N-co-doped hollow carbon polyhedrons, *Chem. Eng. J.* 426 (2021) 130808–130818, <https://doi.org/10.1016/j.cej.2021.130808>.
- [25] X.M. Dang, R.Y. Yang, Z. Wang, S.Y. Wu, H.M. Zhao, Efficient visible-light activation of molecular oxygen to produce hydrogen peroxide using P doped g-C3N4 hollow spheres, *J. Mater. Chem. A* 8 (2020) 22720–22727, <https://doi.org/10.1039/d0ta07794a>.
- [26] D.S. Yang, D. Bhattacharjya, Y.S. Min, J.S. Yu, Highly efficient metal-free phosphorus-doped platelet ordered mesoporous carbon for electrocatalytic oxygen reduction, *Carbon* 67 (2014) 736–743.
- [27] L. Xue, H. Sun, Q. Wu, W. Yao, P-doped melon-carbon nitride for efficient photocatalytic H2O2 production, *J. Colloid Interface Sci.* 615 (2022) 87–94, <https://doi.org/10.1016/j.jcis.2022.01.107>.
- [28] Y. Zhang, J. Yuan, L. Zhao, B. Wu, B. Zhang, P. Zhang, S. Zhang, C. Dong, Boosting exciton dissociation and charge transfer in P-doped 2D porous g-C3N4 for enhanced H2 production and molecular oxygen activation, *Ceram. Int.* 48 (2022) 4031–4046, <https://doi.org/10.1016/j.ceramint.2021.10.193>.
- [29] N. Zheng, X. He, R. Hu, W. Guo, Z. Hu, Co-activation of persulfate by cation and anion from FeP for advanced oxidation processes, *Appl. Catal. B: Environ.* 298 (2021) 120505, <https://doi.org/10.1016/j.apcatb.2021.120505>.
- [30] L. Li, L. Xu, Z. Hu, J.C. Yu, Enhanced Mass Transfer of Oxygen through a Gas-Liquid-Solid Interface for Photocatalytic Hydrogen Peroxide Production, *Adv. Funct. Mater.* 31 (2021) 2106120, <https://doi.org/10.1002/adfm.202106120>.
- [31] L. Li, Z. Hu, J.C. Yu, On-Demand Synthesis of H2O2 by Water Oxidation for Sustainable Resource Production and Organic Pollutant Degradation, *Angew. Chem. Int. Ed.* 59 (2020) 20538–20544, <https://doi.org/10.1002/anie.202008031>.
- [32] L. Xu, Y. Liu, L. Li, Z. Hu, J.C. Yu, Fabrication of a Photocatalyst with Biomass Waste for H2O2 Synthesis, *ACS Catal.* 11 (2021) 14480–14488, <https://doi.org/10.1021/acscatal.1c03690>.
- [33] J.Z. Hu, M.S. Solum, C.M.V. Taylor, R.J. Pugmire, D.M. Grant, Structural determination in carbonaceous solids using advanced solid state NMR techniques, *Energy Fuels* 15 (2001) 14–22, <https://doi.org/10.1021/ef0001888>.
- [34] Z.F. Hu, Z.R. Shen, J.C. Yu, Converting Carbohydrates to Carbon-Based Photocatalysts for Environmental Treatment, *Environ. Sci. Technol.* 51 (2017) 7076–7083, <https://doi.org/10.1021/acs.est.7b00118>.
- [35] J. Zhang, J. Lang, Y. Wei, Q. Zheng, L. Liu, Y.-H. Hu, B. Zhou, C. Yuan, M. Long, Efficient photocatalytic H2O2 production from oxygen and pure water over graphitic carbon nitride decorated by oxidative red phosphorus, *Appl. Catal. B: Environ.* 298 (2021) 120522–120530, <https://doi.org/10.1016/j.apcatb.2021.120522>.
- [36] H. Zhang, S. Chen, Rapid Determination of Total Phosphorus in Water by Microwave Digest/Ammonium Molybdate Spectrophotometry, *Environ. Sci. Technol.* 26 (2003) 19–20.
- [37] J. Zhang, G. Zhang, Q. Ji, H. Lan, J. Qu, H. Liu, Carbon nanodot-modified FeOCl for photo-assisted Fenton reaction featuring synergistic in-situ H2O2 production and activation, *Appl. Catal. B: Environ.* 266 (2020) 118665–118672, <https://doi.org/10.1016/j.apcatb.2020.118665>.
- [38] K. Fuku, R. Takioka, K. Iwamura, M. Todoroki, K. Sayama, N. Ikenaga, Photocatalytic H2O2 production from O2 under visible light irradiation over phosphate ion-coated Pd nanoparticles-supported BiVO4, *Appl. Catal. B: Environ.* 272 (2020) 119003–119010, <https://doi.org/10.1016/j.apcatb.2020.119003>.
- [39] Y. Wang, H. Song, J. Chen, S. Chai, L. Shi, C. Chen, Y. Wang, C. He, A novel solar photo-Fenton system with self-synthesizing H2O2: Enhanced photo-induced catalytic performances and mechanism insights, *Appl. Surf. Sci.* 512 (2020) 145650–145661, <https://doi.org/10.1016/j.apsusc.2020.145650>.
- [40] J. Shi, Z. Liu, Y. Luo, C. Guo, Y. Li, T. Yang, C. Ju, H. Wang, X. Li, Z. Fan, Enhanced photocatalytic production of hydrogen peroxide via two-channel pathway using modified graphitic carbon nitride photocatalyst: Doping K+ and combining WO3, *Colloids Surf. A: Physicochem. Eng. Asp.* 623 (2021) 126758–126768, <https://doi.org/10.1016/j.colsurfa.2021.126758>.
- [41] X.S. Sun, L. Li, S. Jin, W. Shao, H. Wang, X.D. Zhang, Y. Xie, Interface boosted highly efficient selective photooxidation in Bi3O4Br/ Bi2O3 heterojunctions, *Escience* 3 (2023), <https://doi.org/10.1016/j.esci.2023.100095>.
- [42] L. Zhang, S. Wang, C. Ni, M. Wang, S. Wang, Ozone elimination over oxygen-deficient MnOx based catalysts: Effect of different transition metal dopants, *Chem. Eng. Sci.* 229 (2021) 116011–116019, <https://doi.org/10.1016/j.ces.2020.116011>.
- [43] F. Parrino, S. Livraghi, E. Giamello, R. Ceccato, L. Palmisano, Role of hydroxyl, superoxide, and nitrate radicals on the fate of bromide ions in photocatalytic TiO2 suspensions, *ACS Catal.* 10 (2020) 7922–7931, <https://doi.org/10.1021/acscatal.0c02010>.
- [44] Y.F. Zhang, J.H. Fan, B. Yang, W.T. Huang, L.M. Ma, Copper-catalyzed activation of molecular oxygen for oxidative destruction of acetaminophen: The mechanism and superoxide mediated cycling of copper species, *Chemosphere* 166 (2017) 89–95, <https://doi.org/10.1016/j.chemosphere.2016.09.066>.